Andreev bound states probed in three-terminal quantum dots

J. Gramich, A. Baumgartner,[*] and C. Schönenberger

Department of Physics, University of Basel, Klingelbergstrasse 82, CH-4056 Basel, Switzerland

(Received 4 December 2016; revised manuscript received 10 October 2017; published 9 November 2017)

Andreev bound states (ABSs) are well-defined many-body quantum states that emerge from the hybridization of individual quantum dot (QD) states with a superconductor and exhibit very rich and fundamental phenomena. We demonstrate several electron transport phenomena mediated by ABSs that form on three-terminal carbon nanotube (CNT) QDs, with one superconducting (S) contact in the center and two adjacent normal-metal (N) contacts. Three-terminal spectroscopy allows us to identify the coupling to the N contacts as the origin of the Andreev resonance (AR) linewidths and to determine the critical coupling strengths to S, for which a ground state (or quantum phase) transition in such S-QD systems can occur. In addition, we ascribe replicas of the lowest-energy ABS resonance to transitions between the ABS and odd-parity excited QD states, a process we call excited state ABS resonances. In the conductance between the two N contacts we find a characteristic pattern of positive and negative differential subgap conductance, which we explain by considering two nonlocal processes, the creation of Cooper pairs in S by electrons from both N terminals, and a transport mechanism we call resonant ABS tunneling, possible only in multiterminal QD devices. In the latter process, electrons are transferred via the ABS without effectively creating Cooper pairs in S. The three-terminal geometry also allows spectroscopy experiments with different boundary conditions, for example by leaving S floating. Surprisingly, we find that, depending on the boundary conditions and the device parameters, the experiments either show single-particle Coulomb blockade resonances, ABS characteristics, or both in the same measurements, seemingly contradicting the notion of ABSs replacing the single-particle states as eigenstates of the QD. We qualitatively explain these results as originating from the finite time scale required for the coherent oscillations between the superposition states after a single-electron tunneling event. These experiments demonstrate that three-terminal experiments on a single complex quantum object can also be useful to investigate charge dynamics otherwise not accessible due to the very high frequencies.

I. INTRODUCTION

Nanoscale electronic devices in contact with superconducting contacts (S) exhibit a large variety of fundamental physical phenomena and play, for example, a central role in schemes for quantum computation [1,2]. If S is in contact with the many quantum channels of a normal metal (N), phase-coherent Andreev reflections lead to electron pairing and an induced superconducting gap in N. This proximity effect has recently been demonstrated also for one-dimensional semiconducting nanowires [3], where strong spin-orbit interactions can give rise to Majorana bound states [4–6]. If S is strongly coupled to a single-channel quantum dot (QD), new subgap eigenstates form, which are known as Andreev bound states (ABS) [7–10]. ABSs carry the supercurrent in Josephson junctions [11–18], and thus constitute a model system to investigate the superconducting proximity effect in QDs [19]. ABSs might also be exploited as Andreev quantum bits [20,21] and have recently attracted considerable attention in both theoretical [19,22–30] and experimental work [8–10,21,31–37].

Previous experiments on ABSs were focused on QDs with two contacts [8–10,31–35], and only few were possible in multiterminal devices [36,37]. Three-terminal ABS devices allow for new transport mechanisms, so that nonlocal processes like Cooper-pair splitting [38–41] compete with local mechanisms like Andreev tunneling [42]. Such mechanisms are expected to result in new effects like the triplet blockade [26], characteristic

patterns in the electrical conductance [25,28], and other nonlocal effects [29,30]. In addition, even the most basic ABS characteristics are expected to be determined by the barrier strengths, such as the ABS resonance broadening [9,35] and whether a quantum phase transition in the S-QD many-body ground state occurs as a function of the gate and bias voltages. However, the coupling strengths can only be accessed unambiguously in three-terminal geometries [43–46].

Here, we report experiments on three-terminal QD devices fabricated on carbon nanotubes (CNTs) with one central superconducting contact inducing ABSs on the QD. A scanning electron microscopy (SEM) image is shown in Fig. 1. We investigate three devices with different coupling strengths Γ_S to S to investigate several of these open questions and demonstrate a series of new effects and measurement configurations. We use Pb as superconductor, which results in
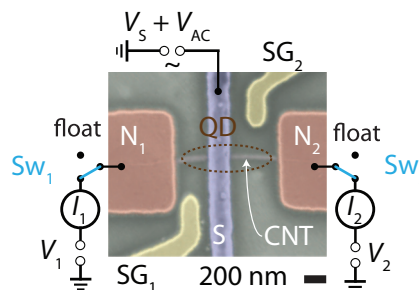

FIG. 1. False-color SEM image of a typical device and schematic of the measurement setup.

[*]andreas.baumgartner@unibas.ch

a large energy gap Δ and thus in a high relative spectroscopic resolution [47], crucial for our experiments. The paper is structured as follows: In Sec. II we summarize our intuitive picture of ABSs and ABS-mediated electron transport in two-terminal devices. Section III describes the sample fabrication and measurement setup. Then, we characterize each of the investigated devices by transport spectroscopy in Sec. IV, from which we extract the tunnel coupling strengths to the individual contacts and demonstrate that Γ_S determines the system ground state and ABS dispersion, while the coupling strengths to the normal-metal contacts, $\Gamma_{1,2}$, determine the spectroscopic width of the Andreev resonances (ARs) [19,28]. One device shows replicas of the lowest-energy ABS resonance at higher energies, which we ascribe to transitions to excited odd-parity QD states in Sec. V. In Sec. VI, we analyze the transport between the two normal-metal contacts mediated by ABSs, in which competing local and nonlocal transport mechanisms give rise to a characteristic pattern of positive and negative differential conductance. These findings are well captured by a simple rate-equation model, which allows us to identify Cooper-pair splitting [38,40] and a three-terminal subgap process we call *resonant ABS tunneling*. In Sec. VII, we show that depending on the boundary conditions imposed in the experiments, the measured conductance either exhibits ABS or Coulomb blockade characteristics, or both at the same time, which we tentatively attribute to finite-frequency coherent oscillations between the single-particle basis states when an ABS is excited by single-electron tunneling.

II. ABS-MEDIATED TWO-TERMINAL TRANSPORT

For illustration and to establish the terms used below, we consider a QD with a single, spin-degenerate level strongly tunnel coupled to a superconductor with a strength Γ_S, and weakly to a normal contact. The former can couple even-charge states of the isolated QD by exchanging Cooper pairs to form new eigenstates of the S-QD system. For $\Delta \to \infty$ (superconducting atomic limit), the emerging ABS can be written as a superposition of the even (empty and doubly occupied) charge states of the isolated QD, i.e., as a singlet eigenstate $|-\rangle = u\,|0\rangle - v^*\,|\!\uparrow\downarrow\rangle$, with u and v the gate-dependent Bogoliubov–de Gennes (BdG) amplitudes and E_- the corresponding eigenenergy. The orthogonal eigenstate at higher energies reads as $|+\rangle = v\,|0\rangle + u^*\,|\!\uparrow\downarrow\rangle$. In contrast, the odd-charge states remain unperturbed doublets $|\sigma\rangle$, with $\sigma = \{\uparrow,\downarrow\}$ and energies E_σ [19,22–24,27]. We note that a similarly intuitive picture can be drawn in the limit of small Δ, in which unpaired QD electrons can form Yu-Shiba-Rusinov singlet states with quasiparticles in the superconductor at energies below the gap and with transport processes formally very similar to the ones discussed below [48,49]. Here, we choose the large-Δ limit for the discussion because of its simple analytical expressions.

The low-energy excitation spectrum of the S-QD system in the large-Δ limit is depicted schematically in Figs. 2(a) and 2(b), for the case of the doublet being the ground state (GS) and the ABS the excited state (ES). Due to the different parity of the doublet and the ABS, one can directly probe the excitation spectrum by single-electron spectroscopy using a weakly coupled normal-metal tunnel probe (N) in an N-QD-S
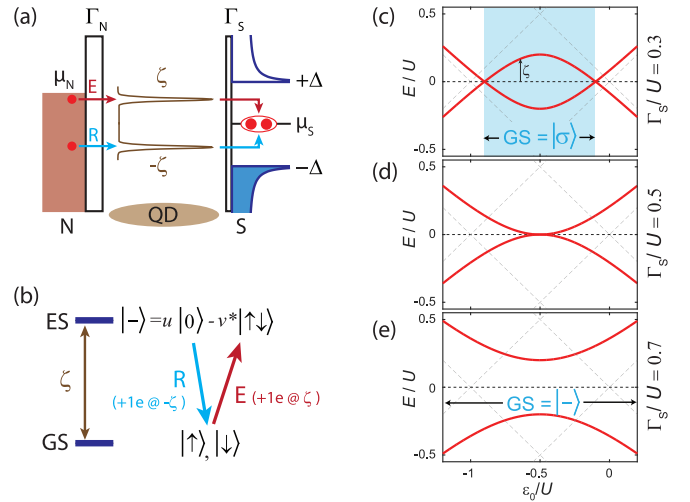

FIG. 2. (a) Schematic of an ABS-mediated two-terminal transport process: an electron at the energy ζ excites the S-QD system (E) and a subsequent electron at $-\zeta$ allows the system to relax again (R), thereby adding a Cooper pair to S. (b) Energy diagram of the excitation and relaxation processes. (c)–(e) ABS resonance energy ζ for $\Delta \to \infty$ as a function of the level position ϵ_0 for $\Gamma_S/U = 0.3$, 0.5, and 0.7, respectively.

geometry [8,10,35,36]. A current through such a device is only possible if the bias matches the Andreev addition energy $\zeta = |E_- - E_\sigma|$, i.e., if the electrochemical potential μ_N of N exceeds (lies below) the excitation energy $+\zeta$ ($-\zeta$) with respect to the electrochemical potential in S, μ_S. As illustrated in Figs. 2(a) and 2(b), charge is transported by an electron tunneling from N into the $|\!\uparrow\downarrow\rangle$ part of $|-\rangle$, which excites (E) the S-QD system from the GS $|\sigma\rangle$ to the ES $|-\rangle$. In a two-terminal device, the system can relax (R) back to the GS only by absorbing a second electron from N at a negative energy $-\zeta$ tunneling into the $|0\rangle$ part of $|-\rangle$, and the transfer of a Cooper pair to S. The probability of this process cycle scales with u^2v^2 [36]. For a reversed bias, a Cooper pair is removed from S. Since in this process two electrons are transferred from N to S we call the resulting subgap conductance features *Andreev resonances* (ARs), which can be seen as a generalization of Andreev reflection found in noninteracting systems.

The ARs show a characteristic gate and bias dependence in the shape of "loops" that directly reflect the competition between superconducting pairing and the Coulomb repulsion on the QD [19]. While deep in the even QD charge states, the GS of the system is the singlet $|-\rangle$ ($E_- < E_\sigma$), in the odd-charge state the charging energy U favors the doublet $|\sigma\rangle$ as GS ($E_\sigma < E_-$), in competition with the pairing induced by Γ_S. As illustrated for the limit $\Delta \to \infty$ in Figs. 2(c)–2(e), one finds for small enough Γ_S [Fig. 2(c)] a gate-tunable transition from $|-\rangle$ to $|\sigma\rangle$ at gate voltages where the AR loops intersect ($\zeta = 0$). In contrast, for large Γ_S the AR loops do not intersect and the GS is always a singlet, as shown in Fig. 2(e). In the large-gap limit $\Delta/\Gamma_S \to \infty$, the critical parameter is Γ_S/U with a GS transition occurring for $\Gamma_S/U < 0.5$ [19,22–24,50,51] [see Fig. 2(d)]. The limit for a phase transition should be reduced for finite Δ due to a competition between the superconducting pairing and

the formation of a Kondo singlet with the quasiparticles at Δ [23,24]. In the strong-coupling limit with $\Delta/\Gamma_S \lesssim 0.5$ theoretical results suggest the following relation for a GS transition to occur:

$$k_B T_{KS}/\Delta \lesssim C, \qquad (1)$$

where the Kondo temperature $k_B T_{KS} \approx \sqrt{\frac{U\Gamma_S}{2}} \exp\left(-\frac{\pi U}{8\Gamma_S}\right)$ characterizes the coupling to S at the electron-hole symmetry point. The number C varies considerably in the literature, between $C \approx 0.4$ and $C \approx 0.79$ in Ref. [52], $C \approx 0.6$ in Ref. [53], and $C \approx 0.73$ in Ref. [23] (values corrected for different definitions of T_K). In the normal state we expect that the Kondo temperature T_K is obtained by replacing Γ_S by the total coupling $\Gamma = \Gamma_1 + \Gamma_2 + \Gamma_S$, where we already included the coupling to a third normal-metal terminal. Although not experimentally demonstrated, yet, our intuitive picture suggests that the spectroscopic width of an AR line in the superconducting state at a bias $eV \ll \Delta$ is determined by the lifetime of the excited state and thus by the finite coupling strength of the QD to all normal terminals $\Gamma_N = \Gamma_1 + \Gamma_2$ (see also Refs. [9,28]).

III. DEVICE FABRICATION AND MEASUREMENT SETUP

We have fabricated CNT three-terminal devices with a lead (Pb) based central $\sim$200 nm wide Pd/Pb/In (4.5–6/110/20 nm) S contact [47], two Pd N contacts and two side gates (SGs) using close to residue free-electron beam lithography [54]. The typical critical perpendicular field for these S contacts is $\sim$200 mT and we apply 400 mT for our normal-state experiments. The highly p-doped Si/SiO$_2$ substrate serves as a back gate (BG). An SEM image of a typical device is shown in Fig. 1, which also illustrates our measurement setup: a dc voltage V_S with a superimposed ac modulation of $\delta V_{ac} = 10\,\mu$V is applied to S, while measuring the variations $\delta I_{1,2}$ in the currents $I_{1,2}$ through the normal terminals N1 and N2 using standard lock-in techniques, which results in the differential conductances $G_{1,2} = \delta I_{1,2}/\delta V_{ac}$. In addition, we can set the potentials on N1 and N2 by the voltages V_1 and V_2, respectively (not shown), or leave them floating individually by the switches Sw$_{1(2)}$ outside the cryostat. Similarly, we can also apply the bias to N1 while measuring the current variations in S and N2, or while leaving S floating. All measurements were performed in a dilution refrigerator at a base temperature of $\sim$35 mK.

We discuss three CNT devices A, B, and C, each exhibiting subgap ARs. In device A, the Pd wetting layer was 4.5 nm thick, while in the devices B and C it was 6 nm. The room-temperature resistances between an N terminal and S were $\sim$30–40 kΩ (sample A) and $\sim$20 kΩ (samples B and C).

IV. S-QD GROUND STATE AND LIFETIMES

In this section, we investigate ABS-mediated transport between N and S terminals in the three devices and take full advantage of the three-terminal geometry. Primarily, we focus on extracting the superconducting energy gap Δ, the charging energy U, and the individual tunnel coupling strengths of the three contacts to the QD and on relating them to the observed AR resonance patterns and the AR broadening. The

relevant data for device A are shown in Fig. 3, device B in Fig. 4, and device C in Fig. 5 and will be discussed in the following subsections. In all figures, we plot the differential conductances G_1 [left, figures (a) and (c)] and G_2 [right, figures (b) and (d)] as a function of a gate voltage and the bias applied to S, V_S, while keeping $V_1 = V_2 = 0$ and $V_{BG} = 0$. The top panels [figures (a) and (b)] show the data for S in the normal state obtained by applying a magnetic field of $B = 0.4$ T perpendicular to the substrate, and the bottom panels [figures (c) and (d)] the measurements with S in the superconducting state at $B = 0$. The relevant extracted and derived device parameters are summarized in Table I.

A. Device A

In Appendix A, we demonstrate in detail that the transport between all three terminals of device A is governed by a single QD. This is also evident in Figs. 3(a) and 3(b), which show the same Coulomb blockade (CB) diamond pattern (dashed lines) in G_1 and G_2 as a function of the bias and the voltage $V_{SG1+2} = V_{SG1} = V_{SG2}$ applied to both SGs, with an even-odd shell-filling sequence in both simultaneously recorded conductance maps. In the odd diamonds, we find horizontal conductance ridges (K, white arrows) due to Zeeman-split Kondo resonances [55,56]. For increasing magnetic fields (not shown), we observe a Zeeman splitting of these ridges with a g-factor of $g \approx 2.1$. Using additional measurement configurations [44], e.g., with the bias applied to an N terminal, we find that the Kondo resonance solely originates from the S contact (not shown).

We first analyze the normal-state data in Figs. 3(a) and 3(b). From the CB resonances we deduce a lever arm $\alpha_{SG1+2} \approx 0.01$ of the combined side gates, a charging energy of $U \approx 2.5$ meV, and from excited state and inelastic cotunneling lines
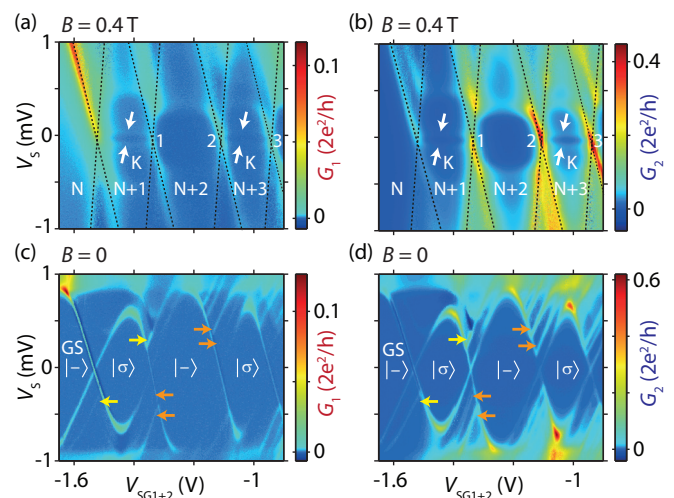

FIG. 3. (a)–(d) Differential conductances G_1 and G_2 of device A as a function of the bias applied to S, V_S, and the voltage V_{SG1+2} applied to both side gates, for $V_{BG} = 0$ and the external magnetic field $B = 0.4$ T [(a), (b)] or $B = 0$ [(c), (d)]. The white arrows in (a) and (b) point out Zeeman-split Kondo resonances (K) and the numbers indicate the zero-bias CB resonances used for fitting. Yellow and orange arrows highlight excited state Andreev resonances.

the lowest two orbital energies ~ 0.3 meV and ~ 0.5 meV. The three-terminal geometry allows one to determine the coupling strengths Γ_i of the individual contacts to the QD by fitting a Breit-Wigner line shape [57] to different two-terminal conductances [43]. This procedure is explained in more detail in Appendix A. From these fits, we obtain $\Gamma = \Gamma_1 + \Gamma_2 + \Gamma_S = 204$ μeV, $\Gamma_S = 150$ μeV, $\Gamma_1 = 1$ μeV, and $\Gamma_2 = 53$ μeV and thus $\Gamma_N = \Gamma_1 + \Gamma_2 = 54$ μeV for resonance 1 in Fig. 3(a). For resonance 2 we obtain $\Gamma = 220$ μeV, $\Gamma_S = 173$ μeV, $\Gamma_1 = 1$ μeV, and $\Gamma_2 = 46$ μeV and thus $\Gamma_N = 47$ μeV, and for resonance 3 $\Gamma = 151$ μeV, $\Gamma_S = 118$ μeV, $\Gamma_1 = 3$ μeV, and $\Gamma_2 = 30$ μeV, so that $\Gamma_N = 33$ μeV. We note that generally $\Gamma_S \gg \Gamma_N$. We estimate the Kondo temperature using $k_B T_K \approx \sqrt{\frac{U\Gamma}{2}} \exp(-\frac{\pi U}{8\Gamma})$ at the electron-hole symmetry point in the middle of the odd diamonds [8,32,58], which, for example, results for resonance 2 in $k_B T_K \approx 6$ μeV ($T_K \approx 70$ mK), expected to be dominated by the temperature broadening [59].

If S is superconducting, as shown in Figs. 3(c) and 3(d), G_1 and G_2 both exhibit a gap $\Delta \approx 0.95$ meV, with pronounced subgap resonances for $|eV_S| \leqslant \Delta$. Also here, we find the same conductance features (though of differing amplitudes) in G_1 and G_2. We discuss the higher-energy replicas of the low-energy AR pointed out by yellow and orange arrows in Figs. 3(c) and 3(d) in Sec. V. The subgap features are fully consistent with ARs: for even spin states (no Kondo ridge in the normal state) we observe large loops, while for odd occupation the loops are smaller and intersect inside the normal-state CB diamonds. This dispersion is characteristic for ARs with a relatively small coupling to S. For example, comparing the extracted system parameters for resonance 2 results in $\Delta/\Gamma_S \approx 5.5$, i.e., the large-$\Delta$ limit, in which $\Gamma_S/U \approx 0.07 \ll 0.5$ suggests a gate-tunable GS transition, consistent with the loop structure observed in the experiments. We note that also the strong-coupling expression predicts a GS transition $k_B T_{KS}/\Delta \approx 1.7 \times 10^{-3} \ll C$ for all C in the literature. Similar results for the other resonances are summarized in Table I and are also consistent with the observed loop structures.

The full width at half the maximum (FWHM) of the three ARs in this device is ~ 50–70 μeV, much smaller than the total coupling strength $\Gamma \sim 0.2$ meV (see Fig. 13 in Appendix A), but consistent with the coupling $\Gamma_N \approx 50$ μeV to the two normal leads. This demonstrates that $\Gamma_N = \Gamma_1 + \Gamma_2$ fully accounts for the ABS excitation lifetime, as expected for $\Gamma_N \ll \Delta$, which holds for all devices investigated here.

B. Device B

In device B, a single QD is formed mainly between S and N1, while the CNT segment between S and N2 shows an essentially gate-independent conductance in an open regime and can be viewed as a contact to the QD. This is shown in more detail in Appendix A. In Fig. 4 we therefore plot G_1 and G_2 as a function of V_S and V_{SG1} to keep the other side unperturbed. In the normal state of S, G_1 in Fig. 4(a) exhibits a pattern typical for a QD strongly coupled to the leads, with an even-odd filling that can still be deduced from cotunneling lines. The CB diamonds are outlined by dashed lines. In contrast, G_2 plotted in Fig. 4(b) shows only a small conductance modulation, as expected for highly transparent barriers. In G_1 we find
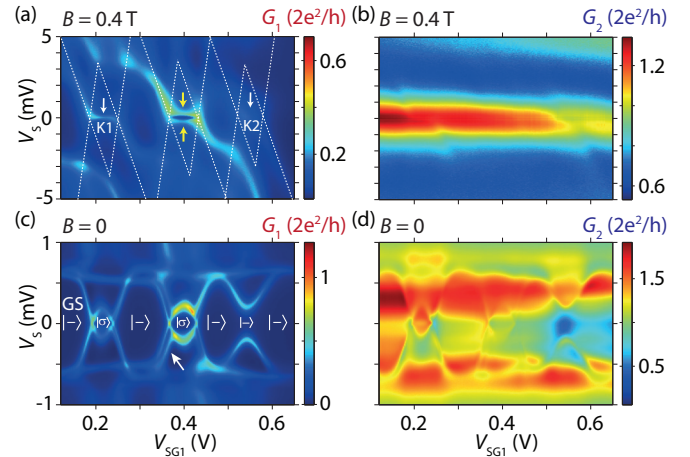

FIG. 4. G_1 and G_2 of device B as a function of V_S and V_{SG1} at $V_1 = V_2 = V_{BG} = V_{SG2} = 0$, for $B = 0.4$ T [(a), (b)] and $B = 0$ [(c), (d)]. The white arrows in (a) label Kondo (K) ridges, and dashed lines qualitatively sketch the CB diamonds, where small (large) diamonds correspond to odd (even) occupation. GS denotes the QD ground state in (c), and the white arrow points to a second Andreev resonance visible at a higher bias $|V_S|$.

Kondo ridges in the odd-charge states (K, arrows), which are strongly broadened so that the Zeeman splitting cannot be resolved. The horizontal lines at $V_S \sim \pm 0.2$ mV in the middle of the conductance map (yellow arrows) do not agree with the expected Zeeman splitting of a (spin) Kondo resonance and $g = 2$ and are probably due to inelastic cotunneling, or due to the valley Kondo effect [60]. From the charge stability diagram in Fig. 4(a) we estimate a lever arm of $\alpha_{SG1} \approx 0.05$, a charging energy of $U \approx 3.0$ meV, and a level spacing of ~ 2.5 meV, consistent with a QD smaller than in device A and located between S and N1. Due to the pronounced Kondo resonances and the strong coupling to the leads, it is difficult to extract the tunnel coupling constants directly. We therefore estimate the coupling strength Γ from the half-width at half maximum (HWHM) of the Kondo ridges K1 and K2 [8,32,61]. We obtain $k_B T_{K1} \approx 0.24$ meV ($T_{K1} \approx 2.8$ K) for K1, and estimate $\Gamma_{K1} \approx 0.8$ meV from $k_B T_K \approx \sqrt{\frac{U\Gamma}{2}} \exp(-\frac{\pi U}{8\Gamma})$ [32]. Similarly, for K2 we find $k_B T_{K2} \approx 0.8$ meV ($T_{K2} \approx 9.3$ K) and $\Gamma_{K2} \approx 1.7$ meV. These values are consistent with the CB resonance width at finite bias and show that the Zeeman splitting of the Kondo resonance can be neglected in this estimate.

G_1 and G_2 for S in the superconducting state are plotted in Figs. 4(c) and 4(d), where we find pronounced ARs in G_1 for bias voltages V_S below the superconducting transport gap $\Delta \approx 0.65$ meV. A weak modulation at the same voltages can also be found in G_2. The AR loop in the leftmost odd state (K1 in the normal state) is considerably smaller than the loops in device A, and the rightmost AR loop (K2 in the normal state) does not exhibit a GS transition at all. The AR between K1 and K2 (arrow) exhibits two resonances related to QD excited states and consistent with normal-state cotunneling lines, as discussed in more detail in Sec. V.

We now use the AR linewidth to estimate the remaining tunneling parameters. Equating the AR linewidths with $\Gamma_N =$

$\Gamma_1 + \Gamma_2$ as established for device A, we find for resonance K1 $\Gamma_N^{K1} \approx 100 \ \mu$eV and $\Gamma_S^{K1} = \Gamma_{K1} - \Gamma_N^{K1} \approx 0.7$ meV, with a corresponding Kondo temperature for the S contact of $k_B T_{KS}^{K1} \approx 190 \ \mu$eV. With $\Delta / \Gamma_S^{K1} \approx 0.93$, this resonance is neither in the large-Δ nor in the strong-coupling limit. However, both expressions still correctly predict a GS transition: $\Gamma_S / U \approx 0.23 < 0.5$ in the large-Δ limit and $k_B T_{KS}^{K1} / \Delta \approx 0.29 < C$ for all mentioned C in the strong-coupling limit. Similarly, we find for resonance K2 $\Gamma_N^{K2} \approx 200 \ \mu$eV and $\Gamma_S^{K2} \sim 1.5$ meV, with $k_B T_{KS}^{K2} = 680 \ \mu$eV. Here, $\Delta / \Gamma_S^{K2} \approx 0.4$, on a scale on which the use of expression 1 is still acceptable. This yields $k_B T_{KS}^{K2} / \Delta \approx 1.1 > C$ for all mentioned C, consistent with a suppression of the GS transition. We note that with $\Delta / \Gamma_S^{K2} \approx 0.5$ the large-Δ limit would predict touching AR loops, on the boundary of the phase transition, in contradiction to the experiment. Qualitatively, the larger coupling of the K2 state results in the suppression of the GS transition, whereas a transition is expected for K1.

C. Device C

In contrast to the devices A and B, device C shows clear characteristics of a double QD with strong interdot coupling (see Appendix A for details). By only varying side gate 1 and keeping $V_{SG2} = 0$, we mostly tune QD1 between N1 and S, while the conductance through QD2 between N2 and S is varied only around the maximum of a QD resonance (Appendix A). For this reason, QD2 can essentially be seen as a contact to QD1. Figures 5(a) and 5(b) show G_1 and G_2 as a function of V_S and V_{SG1} for S in the normal state, with strong cotunneling lines and Kondo resonances in the odd-charge states (K1 and K2). From the charge stability diagram interpolated in Fig. 5(a), we estimate a lever arm of SG1 to QD1 of $\alpha_{SG1} \approx 0.01$, a charging energy of $U \approx 2.4$ meV and a level spacing of ~ 1.3 meV for QD1. Similar as for device B, we estimate Γ from the HWHM of the Kondo resonance and obtain $k_B T_{K1} \approx 0.3$ meV ($T_{K1} \approx 3.5$ K) and $\Gamma_{K1} \approx 0.8$ meV for the resonance K1. For resonance K2 we find $k_B T_{K2} \approx 0.35$ meV ($T_{K2} \approx 4$ K) and $\Gamma_{K2} \approx 0.88$ meV.

For S in the superconducting state, G_1 and G_2 plotted in Figs. 5(c) and 5(d) both show pronounced ARs. In contrast to the previous devices, we find *two* horizontal conductance maxima, one at $\Delta_1 \approx 0.42$ meV most prominent in G_1, and $\Delta_2 \approx 0.75$ meV more clearly visible in G_2, which we tentatively interpret as two superconducting transport gaps in the individual CNT arms. Surprisingly, the ABS loops connect smoothly, but the rightmost loops are bounded by Δ_1, while the leftmost clearly reaches up to Δ_2. Currently, we do not
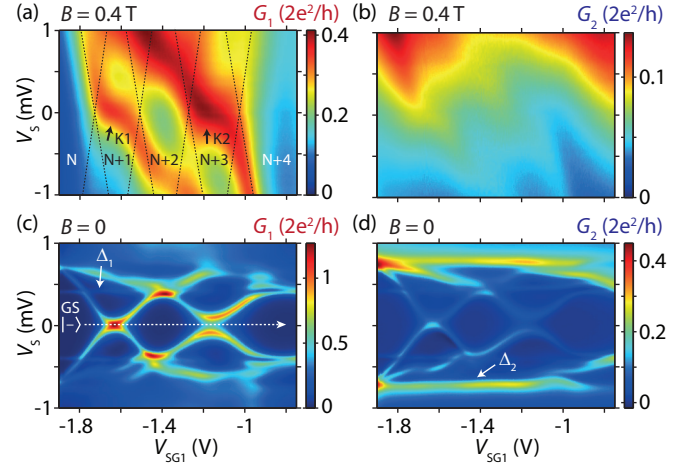

FIG. 5. G_1 and G_2 of device C as a function of V_S and V_{SG1} at $V_1 = V_2 = V_{BG} = V_{SG2} = 0$, for $B = 0.4$ T [(a), (b)] and $B = 0$ [(c), (d)]. The black arrows in (a) label Kondo (K) ridges, and dashed lines sketch the CB diamonds. $\Delta_{1(2)}$ highlight the two superconducting transport gaps.

have a good explanation for these findings, but speculate that the QD wave function might be coupled inhomogeneously to S, e.g., at two separate places with two distinct effective coupling constants. For the present investigation, the relevant findings are that the ABS loops exactly touch for the K1 state and that for K2 the loops are slightly separated in energy, i.e., that the K1 parameters correspond to the critical values of the ABS phase transition and that the GS transition is suppressed for K2.

The latter observations compare well to the extracted tunnel couplings: For device C, we find an AR linewidth of $\Gamma_N \approx 0.1$ meV for both resonances and estimate $\Gamma_S^{K1} \approx 0.7$ meV at the position of the Kondo resonance K1 and $\Gamma_S^{K2} \sim 0.78$ meV for K2. Using Δ_1 as the relevant energy gap, we find $\Delta_1 / \Gamma_S^{K1} \approx 0.60$ for K1 and $\Delta_1 / \Gamma_S^{K2} \approx 0.54$ for K2, both in a range for which it is acceptable to use Eq. (1). The latter results in $k_B T_{KS1} / \Delta_1 \approx 0.57$ for K1, consistent with a "touching" of the AR loops if $C \approx 0.6$ in Eq. (1), and $k_B T_{KS2} / \Delta_1 \approx 0.69$ for K2, suggesting a close but avoided AR loop crossing and no GS transition. We note that the ratios used for the large-Δ limit, $\Gamma_S^{K1} / U \approx 0.29$ for K1 and $\Gamma_S^{K2} / U \approx 0.33$ for K2, would wrongly predict a GS transition for both charge states.

The results of this section are collected in Table I and compared to the AR loop structures found in the experiments. Our experiments clearly suggest a GS transition limit of $C \approx 0.6$ when using Eq. (1). In addition, we find that the

TABLE I. Extracted parameters and observed ABS loop structure for devices A, B, and C. The values for different resonances are separated by a dashed line. Yes is abbreviated by Y, no by N, and crit. means that the AR loops touch.

Device	Δ (meV)	U (meV)	Γ_N (μeV)	Γ_S (μeV)	Δ / Γ_S	Γ_S / U	$k_B T_{KS} / \Delta$	GS transition
A	0.95	2.5	54/47/33	150/173/118	6.3/5.5/8.1	0.06/0.07/0.05	$< 2 \times 10^{-3}$	Y/Y/Y
B	0.65	3.0	100/200	700/1500	0.93/0.43	0.23/0.50	0.29/1.05	Y/N
C	0.42	2.4	100/100	700/780	0.60/0.54	0.29/0.33	0.57/0.69	crit./N

AR broadening is consistent with the coupling to both normal contacts.

V. EXCITED STATE ANDREEV RESONANCES

In Sec. IV we found multiple replicas at higher energies for all ARs in device A and one replica in the central AR of device B. The spacings of $\sim$0.2–0.3 and $\sim$0.5 meV between these replicas are very similar to the spacings of the lowest excited states in the normal-state measurements of this device. We find no such replicas for device C, for which the orbital energies are larger than the superconducting gap, $\delta E > \Delta$. We note that the replicas are not consistent with inelastic Andreev tunneling [42] because they show a clear gate dependence following the lowest AR, we find no negative differential conductance between the resonances, and they are broadened with increasing temperature. In the following, we exploit the third QD terminal to show that the replicas are caused by ABS-mediated transport via excited states of the doublet $|\sigma\rangle$ in the odd QD state, a process we call excited state ARs.

To experimentally identify the origin of these replicas, we performed conductance measurements in a configuration different to the one in Sec. IV. Here, we keep the dc parts $V_1 = V_S = 0$ and apply the dc bias V_2 to N2, while modulating V_S by the ac voltage δV_{ac} (see also Fig. 1 for orientation). We again define the conductances $G_{1,2} = \delta I_{1,2}/dV_{ac}$ from the current modulations in the normal terminals 1 and 2. Figure 6 shows G_1 and G_2 as a function of V_{SG1+2} and V_2. Intuitively, one might expect that G_1 is independent of V_2, which is the case for local processes when neglecting gating effects by V_2. Surprisingly, we find both ABS-mediated ("curved lines") and standard QD resonances ("straight lines") in these data sets. In the picture of $\Delta \to \infty$ this is not trivial and we will discuss this finding in more detail in Sec. VII.

Here, we exploit that the width of both types of transport resonances between N1 and N2 is determined by $\Gamma_1 + \Gamma_2$ only, and not by $\Gamma = \Gamma_1 + \Gamma_2 + \Gamma_S$ as in the normal state (see Sec. IV). This allows us to resolve also excited state resonances between the two N contacts. In Fig. 6 we find both straight lines (labeled by white arrows) and AR with a curved dispersion (orange arrows), best visible in G_2. The straight excited state resonances have a similar spacing as the
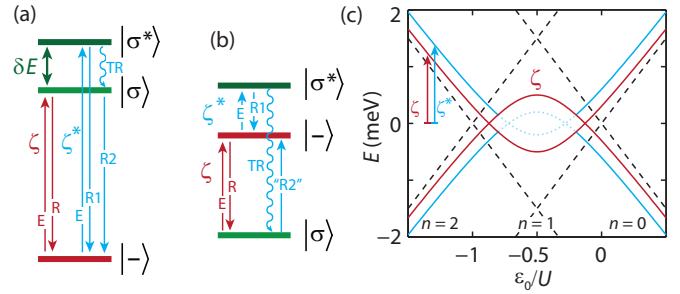
FIG. 7. (a), (b) Expected low-energy charge transitions, including two spin-degenerate single-particle states $|\sigma\rangle$ and $|\sigma^*\rangle$ with a level spacing of δE and the transition energies ζ and ζ^*. TR abbreviates thermal relaxation. Fig. (a) shows the processes for $|-\rangle$ being the GS, (b) the ones for $|-\rangle$ set between $|\sigma\rangle$ and $|\sigma^*\rangle$. (c) ζ and ζ^* as a function of ε_0/U for $U = 3$ meV, $\Gamma_S = 1$ meV, and $\delta E = 0.3$ meV. n denotes the different charge states.

corresponding excited state ARs and sometimes even originate from the same position in these plots.

Excited state ARs can be understood on the same footing as the GS ARs in the $\Delta \to \infty$ limit (Sec. II). In addition to the odd-electron ground state $|\sigma\rangle$, we also consider the corresponding excited state $|\sigma^*\rangle$, separated in energy by δE. As depicted in Fig. 7(a) for $|-\rangle$ being the GS, the system can now also be excited to $|\sigma^*\rangle$ (blue arrows) in addition to $|\sigma\rangle$ (red arrows). The corresponding transition energies ζ^* (blue lines) and ζ (red lines) are plotted in Fig. 7(c). ζ^* replicates the shape of ζ at higher energies, as observed in the experiments. We call the resonances ζ^* *excited state Andreev resonances* because they correspond to a first-order transition between an ABS and an excited odd-electron state. This situation of $|-\rangle$ being the GS results in the excited state AR highlighted by yellow arrows in the experiments of Figs. 3(c) and 3(d). Also consistent with the experiment is that the expected ζ^* line ends at the intersection with ζ in Fig. 7(b), best visible in the central resonance of Fig. 4(c). This can be understood qualitatively by introducing a (fast) energy relaxation from $|\sigma^*\rangle$ to $|\sigma\rangle$, which we call "thermal relaxation" (TR) to distinguish it from the parity-changing relaxation by single-electron tunneling. If $|-\rangle$ is the GS, this results only in a second relaxation channel from $|\sigma^*\rangle$ to the GS, as illustrated in Fig. 7(a). However, if $|\sigma\rangle$ is the GS and $|-\rangle$ lies energetically midway between σ^* and σ or higher, as shown in Fig. 7(b), σ^* can be excited by single electrons at ζ^*, but the system relaxes fast to $|\sigma\rangle$, from where the energy $\zeta > \zeta^*$ is required to reach $|-\rangle$ to close the charge transport cycle. Therefore, we expect for these gate voltages only one resonance at $eV_S = \zeta$, but with an increased amplitude because the additional transport channel via $|\sigma^*\rangle$ is allowed for $eV_S \geqslant \zeta$.

VI. ABS-MEDIATED TRANSPORT BETWEEN TWO N CONTACTS

In three-terminal QD devices, one can expect novel subgap transport mechanisms due to "nonlocal" transport processes that require two N and one S terminal, and their interplay with local effects involving only two terminals [25,28]. In particular, transport between two N contacts can be mediated
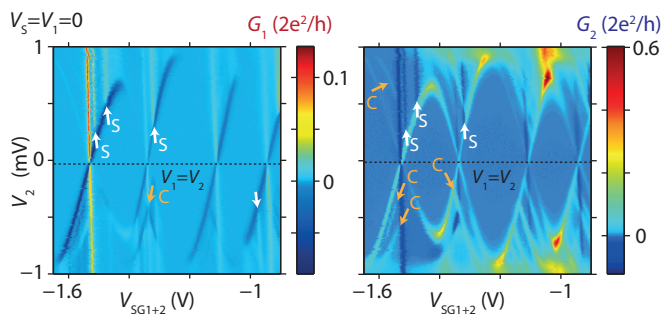

FIG. 6. G_1 and G_2 of device A at $V_{BG} = V_1 = V_S = 0$ as a function of V_2 and a combined side-gate voltage V_{SG1+2} at $V_{S,dc} = 0$. The labels S and C denote partially overlapping straight Coulomb blockade resonances and curved (excited state) ARs, respectively. The horizontal dashed line marks the condition $V_2 = V_1$ [62].
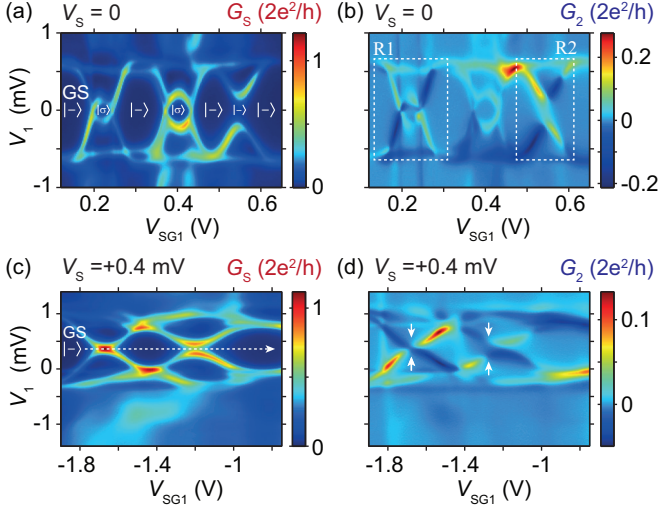
FIG. 8. G_S and G_2 as a function of the applied bias V_1 and the gate voltage V_{SG1}, for (a), (b) device B and $V_S = 0$, (c), (d) device C, and $V_S = +0.4$ mV. Arrows and dashed rectangles mark regions of pronounced conductance sign changes.

by ABSs [28]. To perform this type of experiment, we use a different measurement configuration than in the previous sections, with the ac bias δV_{ac} and the dc bias V_1 applied to N1, while measuring the current variation δI_2 in N2. This can be done while also recording the current variation I_S in S at a fixed potential V_S, or while leaving S floating (see Sec. VII). We again define the differential conductances $G_i = \delta I_i / \delta V_{ac}$.

In Figs. 8(a) and 8(b) we plot G_S and G_2 of device B as a function of V_1 and the gate voltage V_{SG1}, with $V_S = 0$. In addition to the typical AR pattern in G_S already discussed for Fig. 4, we find in G_2 pronounced resonances at the same gate and bias voltages. This illustrates again that N2 is a third terminal to the QD with ABSs. In contrast to the ARs in G_S, the AR amplitudes in G_2 show pronounced sign changes, from positive to negative differential conductance with similar magnitudes $\sim\pm 0.1 \times 2e^2/h$ at positions symmetric around the electron-hole (e-h) symmetry points. The sign is inverted at the e-h symmetry point, at the singlet-doublet GS transitions, and for a reversed bias. This is best visible in the regions R1 and R2 marked by rectangles in Fig. 8(b). The central GS transition deviates from this description, most likely due to the overlapping second AR (see Sec. IV), but also exhibits systematic sign changes. For the devices A and C we find similar characteristics as for device B. As an example, we plot G_S and G_2 of device C in Figs. 8(c) and 8(d), where we added a dc bias $V_S = +0.4$ mV to S. This bias results in an offset of the features in G_S and G_2, where we again find the characteristic sign changes in G_2, labeled by white arrows in Fig. 8(d), identical to region R2 in Fig. 8(b). From these and a series of other measurements with different V_S we conclude that the sign changes are robust against V_S and that all measurements can be understood considering potentials relative to the one on S.

Rate-equation model

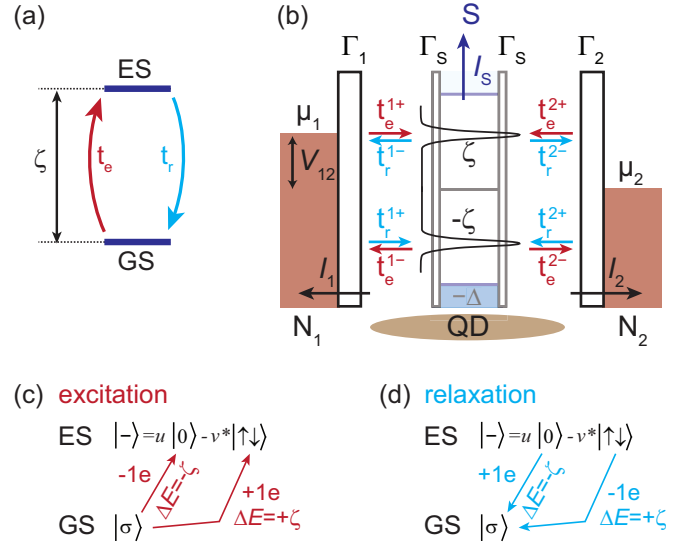To describe the transport through an S-QD system, we introduce a rate-equation model similar to Ref. [36], using the

FIG. 9. (a) Two-level rate-equation model with excitation (relaxation) rate t_e (t_r). (b) Schematic of the three-terminal N-QD-S system, with a faint superimposed S contact, and a negative bias voltage V_1 applied to N1. Transport is only considered through the AR $\pm\zeta$, with color-coded rates $t_{e(r)}^{1(2)+(-)}$. I_1, I_2, and I_S denote the technical current direction in the respective contacts (arrows). (c), (d) Intuitive diagrams of the possible excitation [(c), red] and relaxation [(d), blue] processes and non-vanishing transition matrix elements, if $|\sigma\rangle$ is the GS. We consider only first-order transitions ($+1e/-1e$) with the energy conditions $\Delta E = \pm\zeta$.

$\Delta \to \infty$ limit to describe the ABSs and the doublet states, as shown in Fig. 9(a). The excitation and relaxation rates depend on the transport processes, illustrated in Fig. 9(b). In contrast to the two-terminal case, we now consider a coupling to a third normal-metal terminal N2 with a strength Γ_2, in addition to the terminal S (Γ_S) and N1 (Γ_1). For $E < \Delta$ we need to consider only transport mediated by the ABS. The bias V_1 is applied to N1 as in the experiment, while S and N2 are kept at $\mu_S = \mu_2 = 0$.

The excitation and relaxation rates t_e and t_r denote the total rates by which the system is changed from the GS to the excited state (ES) and back, and will be determined below. The steady-state occupation probabilities P_{GS} and $P_{ES} = 1 - P_{GS}$ of the GS and ES are then found by setting

$$\frac{d}{dt} P_{ES} = t_e P_{GS} - t_r P_{ES} = 0, \qquad (2)$$

which yields $P_{GS} = t_r/(t_r + t_e)$ and $P_{ES} = t_e/(t_r + t_e)$.

The rates t_e and t_r contain all excitation and relaxation processes, which can be viewed in the simplified picture of sequential individual tunneling events, as illustrated in Fig. 9(b). In the corresponding rates we use the superscript 1 (2) to denote the contacts N1 (N2) and $+$ ($-$) to state whether an electron is added (removed) from the S-QD system. The excitation and relaxation rates can then be calculated using Fermi's golden rule [27,36,63]. For example, if $|\sigma\rangle$ is the GS and $|-\rangle$ the ES [see Figs. 9(c) and 9(d)], the rate t_e^{1+} for the

excitation by an electron tunneling in from N1 is

$$|\sigma\rangle \xrightarrow[\text{N1}]{+1e} |-\rangle : \quad t_{\text{e}}^{1+} = \Gamma_1 \underbrace{|\langle -|d_{\bar{\sigma}}^{\dagger}|\sigma\rangle|^2}_{v^2} f_1(\zeta), \quad (3)$$

where $f_{1(2)}(E)$ is the Fermi distribution in contact N1 (N2), $d_{\sigma}^{\dagger}$ (d_{σ}) the creation (annihilation) operator for an electron on the QD with spin σ (opposite spin $\bar{\sigma}$), and v and u are the BdG amplitudes of the ABS. Similarly, we find for the relaxation rate caused by electrons leaving to N2

$$|-\rangle \xrightarrow[\text{N2}]{-1e} |\sigma\rangle : \quad t_{\text{r}}^{2-} = \Gamma_2 \underbrace{|\langle \sigma|d_{\bar{\sigma}}|-\rangle|^2}_{v^2} [1 - f_2(\zeta)]. \quad (4)$$

We note that this latter process is possible only in a three-terminal device. All such excitation and relaxation processes are depicted schematically in Figs. 9(c) and 9(d), which allows to intuitively deduce all tunnel rates. The total excitation and relaxation rates then read as

$$t_{\text{e}} = \underbrace{\Gamma_1 v^2 f_1(\zeta)}_{t_{\text{e}}^{1+}} + \underbrace{\Gamma_2 v^2 f_2(\zeta)}_{t_{\text{e}}^{2+}}$$

$$+ \underbrace{\Gamma_1 u^2 [1 - f_1(-\zeta)]}_{t_{\text{e}}^{1-}} + \underbrace{\Gamma_2 u^2 [1 - f_2(-\zeta)]}_{t_{\text{e}}^{2-}},$$

$$t_{\text{r}} = \underbrace{\Gamma_1 v^2 [1 - f_1(\zeta)]}_{t_{\text{r}}^{1-}} + \underbrace{\Gamma_2 v^2 [1 - f_2(\zeta)]}_{t_{\text{r}}^{2-}}$$

$$+ \underbrace{\Gamma_1 u^2 f_1(-\zeta)}_{t_{\text{r}}^{1+}} + \underbrace{\Gamma_2 u^2 f_2(-\zeta)}_{t_{\text{r}}^{2+}}. \quad (5)$$

For the singlet $|-\rangle$ being the GS, all rates can be obtained from Eq. (5) by replacing u by v because the initial and final states in the transition matrix elements are interchanged. The total currents into N1 and N2 are then given by

$$I_1 = \frac{e}{h} \big[(t_{\text{e}}^{1+} - t_{\text{e}}^{1-}) P_{\text{GS}} + (t_{\text{r}}^{1+} - t_{\text{r}}^{1-}) P_{\text{ES}} \big],$$

$$I_2 = \frac{e}{h} \big[(t_{\text{e}}^{2+} - t_{\text{e}}^{2-}) P_{\text{GS}} + (t_{\text{r}}^{2+} - t_{\text{r}}^{2-}) P_{\text{ES}} \big], \quad (6)$$

and $I_{\text{S}} = -(I_1 + I_2)$. The differential conductance measured at contact $i = \{1, 2, S\}$ can then be obtained as $G_i = dI_i/dV_1$ for the experiments described in this section.

An example of such a calculation is shown in Fig. 10 for parameters that result in the familiar ABS loop structure and positive conductance values in the two-terminal local conductance G_{S}. This is plotted in Fig. 10(b) as a function of V_1 and the normalized gate-tunable QD orbital energy ε_0/U and corresponds, for example, to the resonances in the leftmost region in Fig. 8(a). More importantly, Fig. 10(c) shows G_2 for the same parameter range, which should be compared to the leftmost region R1 in Fig. 8(b). We find that the model at least qualitatively reproduces the experimental findings, with sign changes at the e-h symmetry point ($\varepsilon_0/U = -0.5$) and for a reversed bias, and clearly highlighting the GS transition. Similarly, for large Γ_{S} and $|-\rangle$ being the GS for all gate voltages, we find sign changes only at the e-h symmetry point, consistent with the resonances in the rightmost region R2 in Figs. 8(b) and 8(d). The corresponding plots are shown in Appendix B in Fig. 16. In addition, the sign changes in the
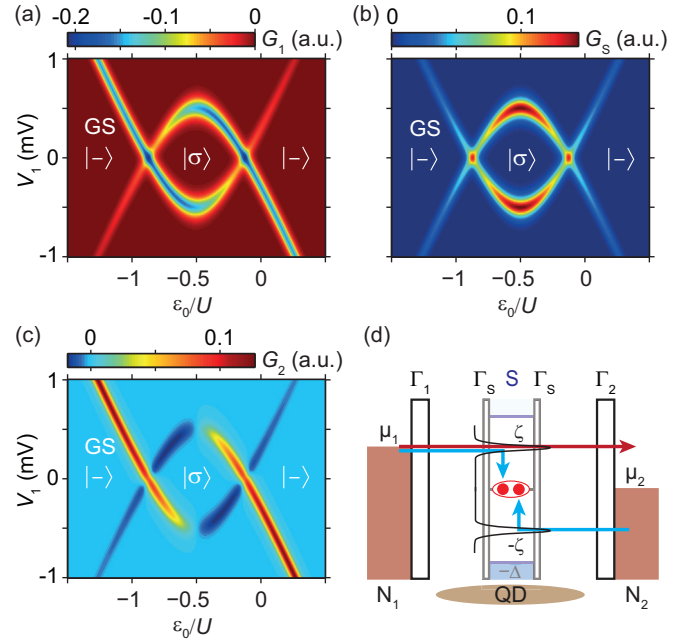

FIG. 10. (a)–(c) Model calculation of the differential conductance according to Eqs. (6) and (5) in the $\Delta \to \infty$ limit, for $\Gamma_{\text{S}} = 1$ meV, $U = 3$ meV, and $\Gamma_1 = \Gamma_2 = 0.1$ meV. (a) G_1, (b) G_{S}, and (c) G_2 as a function of V_1 applied to N1 and the QD orbital energy ε_0/U, for $V_2 = V_{\text{S}} = 0$, as in the experiment. To simulate a broadening of the AR, a small finite temperature of $T = 0.5$ K was assumed. (d) Schematic of the "nonlocal" transport processes for $\mu_1 > +\zeta$. The red arrow depicts "resonant ABS tunneling", i.e., a direct transfer of one electron from N1 to N2 via the ABS, whereas the blue arrows show an inverse CPS process, i.e., the "nonlocal" creation of a Cooper pair in S.

model are independent of the applied voltages V_{S} or V_2, as in the experiment.

Due to the Fermi functions, the only nonvanishing rates at low temperatures are t_{e}^{1+}, t_{r}^{1+}, t_{r}^{2-}, and t_{r}^{2+} for a forward bias $\mu_1 > \mu_{\text{S}} > \mu_2$, as depicted in Fig. 9. For example, the local Andreev processes between N1 and S scale with $t_{\text{e}}^{1+} t_{\text{r}}^{1+}$. More interestingly, the sign changes in G_2 are caused by the competition between processes comprising the two relaxation processes t_{r}^{2-} and t_{r}^{2+}, which remove or add an electron from the system at different energies, respectively. In this case, the current in N2 is proportional to the difference between the BdG amplitudes $I_2 \propto (u^2 - v^2)$, with a sign change at the GS transition (transition from $u^2 > v^2$ to $u^2 < v^2$), or for a reversed bias V_1. The conductance G_2 thus reflects directly the gradual charging of the ABS with decreasing gate voltage, which evolves from an excess charge of 0 in the $n = 0$ state to an average charge of $2e$ in the $n = 2$ state. In a more coherent picture, the process combining an electron tunneling into the system from both N1 and N2 (t_{e}^{1+} combined with t_{r}^{2+}) corresponds to the "nonlocal" creation of a Cooper pair in S, often called (inverse) Cooper-pair splitting (CPS). Similarly, the coherent tunneling into and out of the system at the same energy (t_{e}^{1+} combined with t_{r}^{2-}) corresponds to the direct transfer of one electron from N1 to N2, mediated by the ABS. This process we call "*resonant ABS tunneling*". These nonlocal transport processes involve all three terminals and

are illustrated in Fig. 10(d). For these processes we expect the rates $t_{iCPS} \propto t_e^{1+} t_r^{2+}$ for inverse CPS and $t_{rABSt} \propto t_e^{1+} t_r^{2-}$ for resonant ABS tunneling. This interpretation is also supported by recent more fundamental calculations [25,28], all in good agreement with our experiments and the simple model. We point out that to account for the similar magnitudes of the positive and negative differential conductance in G_2, it is necessary that CPS and resonant ABS tunneling are of similar strength.

VII. COHERENT OSCILLATIONS IN THE ABS

In this section, we present and compare measurements with different boundary conditions imposed to the QD terminals. For example, Figs. 11(a)–11(c) show the differential conductance G between the two normal-metal contacts (see also in the previous section) with the superconductor S left floating. The data for the devices A, C, and B are plotted as a function of the bias and gate voltage in the same gate-voltage intervals as discussed in the previous sections. The data sets are ordered according to increasing Γ_S, as found in Sec. IV. Such experiments are equivalent to Ref. [37], where ABSs in a proximitized S-QD InAs nanowire were investigated in the context of Majorana bound states.

For device A, with a weak coupling to S and a small Γ_S / U ratio, we find CB diamonds very similar to the normal state. Specifically, there are no ARs, nor a suppression of G related to a superconducting gap. ARs were, however, clearly observed when the superconductor was grounded (see Fig. 3), and both types of resonances were found in the experiments of Fig. 6. In contrast, devices C and B, both with a larger coupling to S, show clear signatures of ARs and the energy gap. However, in these experiments no sign changes in G occur and we observe only positive differential conductance features, in stark contrast to S being on a fixed potential (Fig. 8). For device B, this experiment results in essentially the same AR gate and bias dispersion as when measured between an N and the S contact (Fig. 4), whereas for device C we find additional curved resonances at higher energies (cf. Fig. 5). We note that the ARs are centered around zero bias, which suggests that μ_S either follows μ_{N1} or μ_{N2} due to the different coupling strengths to the normal-metal terminals.

The experiments on devices B and C are straightforward to understand qualitatively based on our previous picture of ABSs: we assumed that the CNT segment between N1 and N2 forms a QD in the normal state of S. In the superconducting state, the eigenstates of the segment are ABSs that determine all subgap transport. If S is at a fixed potential, it can take up (or emit) Cooper pairs, which allows Cooper-pair splitting as a process and, in unison with resonant ABS tunneling, results in the pattern of positive and negative differential conductance. If S is floating, the experiments show that μ_S is fixed, and since CPS and the local Andreev processes both add charges to S, which would change the electrical (though not the chemical) potential of S, these processes exactly compensate to satisfy the boundary condition $I_S = 0$. This leaves only resonant ABS tunneling as a subgap transport process between N1 and N2, which does not change the charge on S and results in a positive G, mapping out the ABS excitation energy. Additional features and different amplitudes compared to the traditional ARs are to be expected since here only electrons at one energy are involved and we expect that the balance between the processes that change the charge on S depend on the bias.

The interpretation of the experiments on device A is less obvious. We find in the conductance between N1 and N2 the standard QD resonances when S is floating, while if S is at a fixed potential modulated by the ac voltage, ABS signatures occur simultaneously with the standard QD features (see Fig. 6 in Sec. V). In the two-terminal measurements between N and S, we only find ABS-related signals. These experiments seem quite contradictory since one would expect that the eigenstates of the S-QD system do not depend on the boundary conditions of the measurement. As discussed for samples B and C, the different processes are combined to satisfy the different boundary conditions, but the simultaneous observation of standard Coulomb blockade and ABS features cannot be resolved with such arguments alone.

This suggests that our picture of ABS-mediated transport is not complete and only holds for a strong enough coupling to S. In this picture, we assume that the QD develops new eigenstates due to the coupling to the unperturbed superconductor and one might expect that a continuous lowering of the coupling strengths results in a continuous transition from the
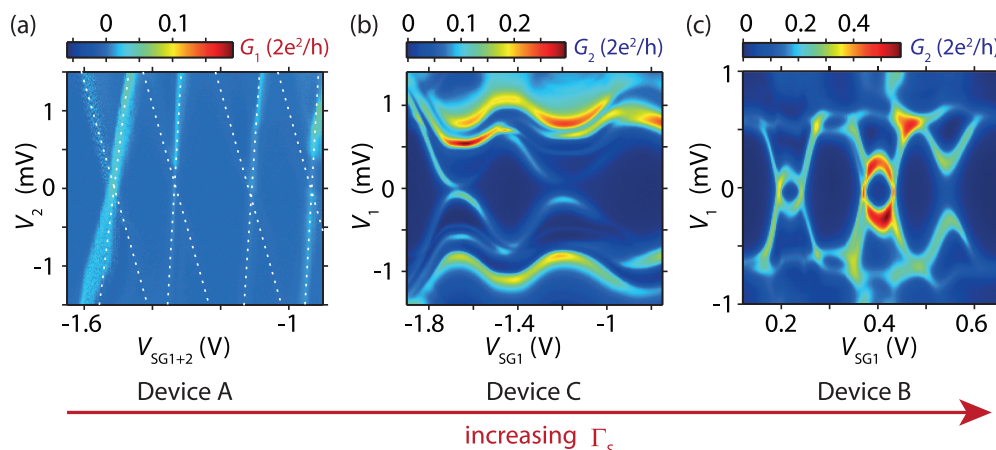

FIG. 11. Conductance between the two normal contacts N1 and N2 with the S contact floating. (a) $G_1(V_2, V_{SG1+2})$ for device A, (b) $G_2(V_1, V_{SG1})$ for device C, and (c) $G_2(V_1, V_{SG1})$ for device B. The measurements are ordered according to increasing coupling strengths Γ_S.

ABS to the bare QD states. In contrast, our results seem to suggest that in some parameter regime, both sets of states are available for different transport processes.

We speculate that for low enough Γ_S the tunneling of an electron on and off the QD from an N terminal is faster than the exchange of Cooper pairs with S, which is necessary for the hybridization of the QD with S. Right after the first tunneling event, the system is in the state $|\uparrow\downarrow\rangle$, which is a coherent superposition of the system eigenstates $|-\rangle$ and $|+\rangle$, i.e., $|\uparrow\downarrow\rangle = -v\,|-\rangle + u\,|+\rangle$ ($|0\rangle = u^*\,|-\rangle + v^*\,|+\rangle$). Therefore, we expect coherent oscillations between $|0\rangle$ and $|\uparrow\downarrow\rangle$ in an ABS excited by single-electron tunneling events, with a characteristic frequency essentially determined by Γ_S. This oscillation is expected to result in a suppression of the waiting time distribution for short times [64], and might be responsible for our findings here: in a three-terminal device, an excitation cannot only be absorbed by forming a Cooper pair, as in a two-terminal device, but also by tunneling out into the third terminal (resonant ABS tunneling). If this happens faster than half a coherent oscillation, the tunneling electron stays in the bare QD state during the time it resides on the CNT segment. Assuming that an oscillation by half a period is required to transfer a Cooper pair to S, we find the relation $\Gamma_{N2} > \Gamma_S/\pi$ as a necessary condition to observe the bare QD resonances, in good agreement with device A, but not for the other two devices with considerably larger Γ_S and a faster oscillation rate relative to Γ_{N2}. Our results demonstrate that a three-terminal QD can give access to the fast electron dynamics, in our example of the ABS coherent oscillations with frequencies Γ_S/h in the range between $\sim$30 GHz (device A) to $\sim$370 GHz (device B), by the implicit comparison to the tunnel rate to the third terminal.

VIII. CONCLUSIONS

In summary, we investigate electronic transport mediated by Andreev bound states in a three-terminal S-QD device and identify the coupling to the normal-metal leads as the main source for the spectroscopic broadening of the Andreev resonances, and establish how the coupling to the superconductor determines the ground state of the system. In addition, we present "excited state Andreev resonances" at higher energies, with transitions between ABSs and odd-parity excited QD states. We also report pronounced sign changes in the ABS-mediated transport between the two normal-metal contacts, which we explain in an intuitive rate-equation model as resulting from the competition between the nonlocal creation of a Cooper pair in S and a process we call "resonant ABS tunneling", i.e., the subgap transport of single electrons through the S-QD system, only allowed in multiterminal devices. Surprisingly, we find that depending on the imposed boundary conditions in the experiments, it is possible to observe either ABSs or Coulomb blockade resonances, or both in the same experiment, which we tentatively attribute to the competition between coherent oscillations in the ABS (exchange of Cooper pairs with S) and the relaxation of the system by single-electron tunneling into the second normal terminal.

We believe that experiments on complex quantum systems using multiple terminals provide a novel and clear experimental probe for many old and new phenomena, here for

example the onset of the superconducting proximity effect on a QD and the formation of many-body quantum states. Such experiments also give direct access to the strength of the coupling between S and the QD, and a way to probe time-dependent phenomena such as the finite-frequency coherent oscillation between superposition states, without resorting to high-frequency and time-domain experiments. In particular, we envisage experiments in similar structures with gate-tunable tunnel barriers [65] to investigate in more depth the presented physical mechanisms.

APPENDIX A: ADDITIONAL DATA FOR DEVICES A, B, AND C

In this Appendix, we analyze additional data of devices A, B, and C. In particular, we discuss the electronic configuration of each device, using conductance maps as a function of both side-gate voltages.

1. Device A

Figures 12(a) and 12(b) show the differential conductances G_1 and G_2 of device A as a function of the side-gate voltages V_{SG1} and V_{SG2}, for the ac bias applied to S, but with $V_S = V_{BG} = 0$, and in the normal state of the device at $B = 0.3$ T. These data are consistent with a single QD [66–68], for example, because we observe the same resonance
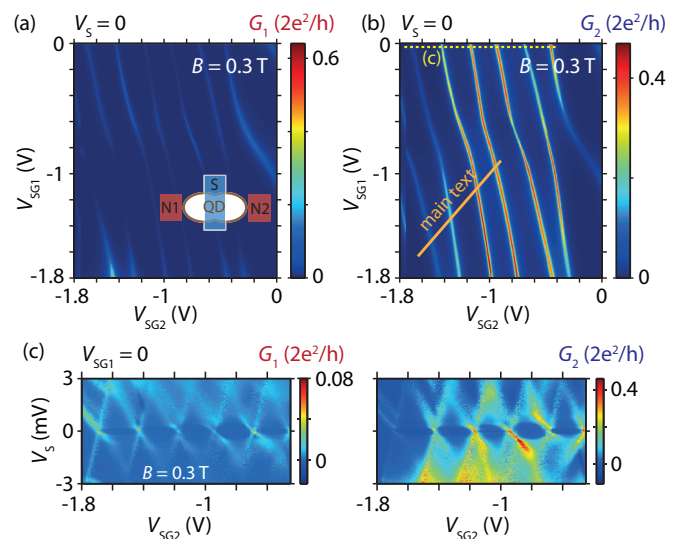

FIG. 12. (a), (b) Differential conductances G_1 and G_2 of device A as a function of the side-gate voltages V_{SG1} and V_{SG2}, for $V_S = V_1 = V_2 = V_{BG} = 0$, at an external magnetic field of $B = 0.3$ T applied out of plane. The orange (dashed yellow) line in (b) indicates the studied gate voltages in the main text [in (c)]. The inset in (a) sketches the assumed electronic QD configuration of the device. (c) G_1 and G_2 as function of V_S and V_{SG2} only, at $B = 0.3$ T and $V_{SG1} = V_1 = V_2 = V_{BG} = 0$.
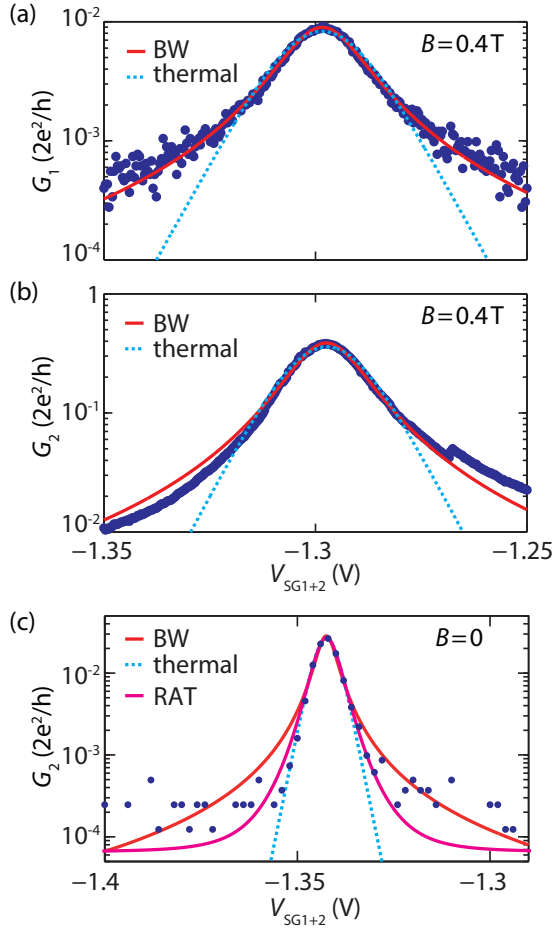
FIG. 13. Differential conductances G_1 (a) and G_2 (b) of resonance 1 (main text) as a function of the combined side-gate voltage V_{SG1+2}, at $V_S = V_1 = V_2 = V_{BG} = 0$ and $B = 0.4$ T, i.e., when S is in the normal state. Red (blue dashed) lines represent the best fit obtained for a Breit-Wigner (BW) [43,57] line shape (thermally broadened) CB resonance. (c) G_2 of resonance 1 at $B = 0$, i.e., when S is superconducting. In addition to fits with a BW and thermally broadened line, we also show the fit to a two-terminal expression for resonant Andreev tunneling (RAT) [42].

lines in both N1 and N2, and when we apply the ac bias to S. In addition, we find one dominant slope of the CB resonances that react similarly to both side gates. There are only vague hints at a more complex confinement potential, possibly due to disorder or potential fluctuations on the substrate, e.g., a slight conductance modulation with some features stronger (weaker) in one (the other) arm, and slight changes in the slopes or the spacing between neighboring resonances. The electronic configuration we qualitatively deduce from these findings is sketched in the inset of Fig. 12(a). In particular, in the region studied in the main text, marked by an orange line in Fig. 12(b), the assumption of a single QD is justified. In Fig. 12(c), we plot the differential conductance in the normal state of S along the yellow dashed line of Fig. 12(b), as a function of the V_S and one side-gate voltage only. Here, we also clearly observe the same diamond structure in both arms of the device, further supporting this claim.

Next, we briefly demonstrate the fitting procedure to determine the individual Γ_i of the contacts. In Fig. 13, the
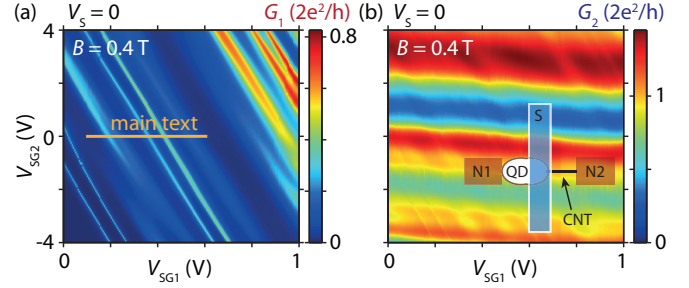

FIG. 14. (a), (b) G_1 and G_2 of device B as a function of the side-gate voltages V_{SG1} and V_{SG2}, for $V_S = V_1 = V_2 = V_{BG} = 0$, at $B = 0.4$ T. The orange line in (a) indicates the studied gate-voltage region in the main text. Inset in (b): assumed electronic configuration of the CNT device.

simultaneously measured zero-bias conductance $G_1 \equiv G_{1S}$ and $G_2 \equiv G_{2S}$ of resonance 1 (main text) is plotted as a function of the gate voltage V_{SG1+2} in the normal state of the device. Fits with a Breit-Wigner line shape for a three-terminal device in the lifetime-broadened limit ($k_B T \ll \Gamma$) and in the single-level transport regime ($k_B T \ll U, \delta E$) with the gate-tunable position E_0 of the resonance [43,57],

$$G_{ij}(E) = \frac{e^2}{h} \frac{\Gamma_i \Gamma_j}{(\Gamma_1 + \Gamma_2 + \Gamma_S)^2/4 + (E - E_0)^2}, \quad \text{(A1)}$$

agree very well with the data, and yield $\Gamma = \Gamma_1 + \Gamma_2 + \Gamma_S \approx 205$ μeV, $\Gamma_S \Gamma_1 \approx 198$ μeV^2, and $\Gamma_S \Gamma_2 \approx 7945$ μeV^2. From these equations, all parameters are determined for $\Gamma_S > \Gamma_1, \Gamma_2$. This assumption can be directly justified from a similar analysis of measurements with the bias applied to N1, while measuring $G_S \equiv G_{S1}$ and $G_2 \equiv G_{21}$ (not shown). In addition, we show in Fig. 13(c) the zero-bias cross section of resonance 1 at $B = 0$, i.e., for S being superconducting. As described in more detail before [42], the resonance is more narrow and better described by resonant Andreev tunneling (RAT). However, the expression used in Fig. 13(c) [42] is meant for two-terminal devices, and accordingly the extracted parameters do not correspond in an obvious way to the ones in the normal state.

2. Device B

Figures 14(a) and 14(b) show G_1 and G_2 of device B as a function of the side-gate voltages V_{SG1} and V_{SG2}, for the ac bias applied to S, but with $V_S = V_{BG} = 0$, and in the normal state of the device at $B = 0.4$ T. In the conductance map of G_1, we observe a single dominant slope which is tuned mostly with V_{SG1}, suggesting a QD located between S and N1. In contrast, G_2 plotted in Fig. 14(b) shows a very high conductance with a weak and slow amplitude variation as function of V_{SG2}, characteristic for a more open CNT regime with highly transmissive contacts. In particular, G_2 never approaches zero. Imprints of the resonances from G_1 can be observed in G_2, which we ascribe to resistive and capacitive crosstalk [38,40]. Hence, we assume an electronic configuration of the CNT device as schematically depicted in the inset of Fig. 14(b), with a larger QD on the left side of the device mostly tunable by V_{SG1}, and an "open" CNT lead to the right.
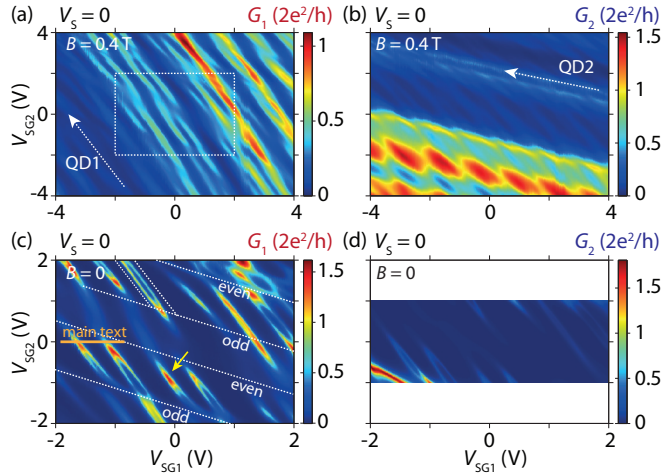
FIG. 15. G_1 and G_2 of device C as a function of the side-gate voltages V_{SG1} and V_{SG2}, for $V_S = V_1 = V_2 = V_{BG} = 0$, at $B = 0.4$ T [(a), (b)] and at $B = 0$ [(c), (d)]. White dashed arrows in (a) and (b) denote different slopes consistent with resonances of QD1 or QD2. The white rectangle marks the region studied in (c) and (d). In (c), the orange line corresponds to the gate-voltage region studied in the main text, and dashed lines denote the charge states of QD2 (even/odd).

3. Device C

In Fig. 15, G_1 and G_2 of device C are plotted as a function of the side-gate voltages V_{SG1} and V_{SG2}, for the ac bias applied to S, but with $V_S = V_{BG} = 0$, for S in the normal state at $B = 0.4$ T [Figs. 15(a) and 15(b)] and in the superconducting state at $B = 0$ [Figs. 15(c) and 15(d)].

In contrast to devices A and B, a charge stability diagram with anticrossings characteristic for a double quantum dot with strong interdot coupling and hybridization is observed in the normal state of S. In Figs. 15(a) and 15(b), the dominant conductance lines with different slopes in G_1 and G_2 are consistent with resonances of QD1 or QD2. An apparent smearing of the resonances in every other charge state, both for QD1 and QD2, is due to pronounced Kondo ridges. In particular, the broad resonances in Fig. 15(a) which we ascribe to QD1 indicate an odd-charge state with a Kondo ridge. This
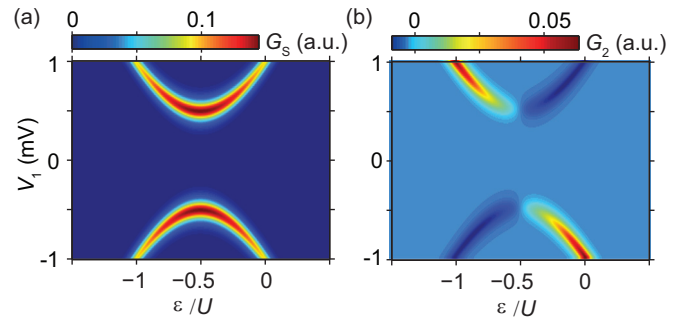

FIG. 16. Model calculation for $\Gamma_S = 2$ meV, $U = 3$ meV, and $\Gamma_1 = \Gamma_2 = 0.1$ meV. (a) Shows G_S and (b) G_2 as a function of V_1 applied to N1 and the QD orbital energy ε_0/U, for $V_2 = V_S = 0$, as in the experiment. To simulate a broadening of the AR, a temperature of $T = 0.5$ K was assumed.

is more obvious when one closely inspects the region indicated by a dashed rectangle in Fig. 15(a) in the superconducting state of S, which is plotted in Fig. 15(c). Here, one observes a pair of Andreev resonance lines in the even-charge state of QD2 (yellow arrow), corresponding to the two singlet-doublet GS transitions observed in the odd-charge states of QD1. These GS transitions vanish close to the boundary and in the odd-charge state of QD2, which can for example be seen by following the Andreev resonances marked with a yellow arrow. In the main text, we focus on Andreev states in QD1 for a fixed even-charge state of QD2, but close to its charge degeneracy point. The corresponding gate-voltage region is indicated by an orange line in Fig. 15(c).

APPENDIX B: MODEL RESULTS FOR LARGE Γ_S

Figure 16 shows the model calculation of the differential conductance according to Eqs. (5) and (6) in the $\Delta \to \infty$ limit for the same parameters as in Fig. 10, but with a twice as large Γ_S. This calculation reproduces at least qualitatively the measurements in region R2 of Fig. 8(b), which shows the data for a large-Γ_S AR.

[1] S. De Franceschi, L. Kouwenhoven, C. Schönenberger, and W. Wernsdorfer, Hybrid superconductor-quantum dot devices, Nat. Nanotechnol. **5**, 703 (2010).

[2] S. D. Sarma, M. Freedman, and C. Nayak, Majorana zero modes and topological quantum computation, NPJ Quantum Inf. **1**, 15001 (2015).

[3] W. Chang, S. M. Albrecht, T. S. Jespersen, F. Kuemmeth, P. Krogstrup, J. Nygård, and C. M. Marcus, Hard gap in epitaxial semiconductor-superconductor nanowires, Nat. Nanotechnol. **10**, 232 (2015).

[4] V. Mourik, K. Zuo, S. M. Frolov, S. R. Plissard, E. P. A. M. Bakkers, and L. P. Kouwenhoven, Signatures of majorana fermions in hybrid superconductor-semiconductor nanowire devices, Science **336**, 1003 (2012).

[5] T. D. Stanescu and S. Tewari, Majorana fermions in semiconductor nanowires: fundamentals, modeling, and experiment, J. Phys.: Condens. Matter **25**, 233201 (2013).

[6] S. M. Albrecht, A. P. Higginbotham, M. Madsen, F. Kuemmeth, T. S. Jespersen, J. Nygård, P. Krogstrup, and C. M. Marcus, Exponential protection of zero modes in majorana islands, Nature (London) **531**, 206 (2016).

[7] A. Eichler, M. Weiss, S. Oberholzer, C. Schönenberger, A. L. Yeyati, J. C. Cuevas, and A. Martín-Rodero, Even-Odd Effect in Andreev Transport through a Carbon Nanotube Quantum Dot, Phys. Rev. Lett. **99**, 126602 (2007).

[8] R. S. Deacon, Y. Tanaka, A. Oiwa, R. Sakano, K. Yoshida, K. Shibata, K. Hirakawa, and S. Tarucha, Tunneling Spectroscopy of Andreev Energy Levels in a Quantum Dot

Coupled to a Superconductor, Phys. Rev. Lett. **104**, 076805 (2010).

[9] J.-D. Pillet, C. H. L. Quay, P. Morfin, C. Bena, A. L. Yeyati, and P. Joyez, Andreev bound states in supercurrent-carrying carbon nanotubes revealed, Nat. Phys. **6**, 965 (2010).

[10] T. Dirks, T. L. Hughes, S. Lal, B. Uchoa, Y.-F. Chen, C. Chialvo, P. M. Goldbart, and N. Mason, Transport through andreev bound states in a graphene quantum dot, Nat. Phys. **7**, 386 (2011).

[11] Y. J. Doh, J. A. van Dam, A. L. Roest, E. Bakkers, L. P. Kouwenhoven, and S. De Franceschi, Tunable supercurrent through semiconductor nanowires, Science **309**, 272 (2005).

[12] J. A. van Dam, Y. V. Nazarov, E. P. A. M. Bakkers, S. de Franceschi, and L. P. Kouwenhoven, Supercurrent reversal in quantum dots, Nature (London) **442**, 667 (2006).

[13] P. Jarillo-Herrero, J. A. van Dam, and L. P. Kouwenhoven, Quantum supercurrent transistors in carbon nanotubes, Nature (London) **439**, 953 (2006).

[14] H. I. Jørgensen, T. Novotný, K. Grove-Rasmussen, K. Flensberg, and P. E. Lindelof, Critical current 0-π transition in designed josephson quantum dot junctions, Nano Lett. **7**, 2441 (2007).

[15] A. Eichler, R. Deblock, M. Weiss, C. Karrasch, V. Meden, C. Schönenberger, and H. Bouchiat, Tuning the josephson current in carbon nanotubes with the kondo effect, Phys. Rev. B **79**, 161407 (2009).

[16] R. Maurand, T. Meng, E. Bonet, S. Florens, L. Marty, and W. Wernsdorfer, First-Order 0-π Quantum Phase Transition in the Kondo Regime of a Superconducting Carbon-Nanotube Quantum Dot, Phys. Rev. X **2**, 011009 (2012).

[17] R. Delagrange, D. J. Luitz, R. Weil, A. Kasumov, V. Meden, H. Bouchiat, and R. Deblock, Manipulating the magnetic state of a carbon nanotube josephson junction using the superconducting phase, Phys. Rev. B **91**, 241401 (2015).

[18] R. Delagrange, R. Weil, A. Kasumov, M. Ferrier, H. Bouchiat, and R. Deblock, 0-π quantum transition in a carbon nanotube josephson junction: Universal phase dependence and orbital degeneracy, Phys. Rev. B **93**, 195437 (2016).

[19] A. Martín-Rodero and A. L. Yeyati, Josephson and andreev transport through quantum dots, Adv. Phys. **60**, 899 (2011).

[20] A. Zazunov, V. S. Shumeiko, E. N. Bratus', J. Lantz, and G. Wendin, Andreev Level Qubit, Phys. Rev. Lett. **90**, 087003 (2003).

[21] C. Janvier, L. Tosi, L. Bretheau, Ç. Ö. Girit, M. Stern, P. Bertet, P. Joyez, D. Vion, D. Esteve, M. F. Goffman *et al.*, Coherent manipulation of andreev states in superconducting atomic contacts, Science **349**, 1199 (2015).

[22] E. Vecino, A. Martín-Rodero, and A. L. Yeyati, Josephson current through a correlated quantum level: Andreev states and π junction behavior, Phys. Rev. B **68**, 035105 (2003).

[23] J. Bauer, A. Oguri, and A. C. Hewson, Spectral properties of locally correlated electrons in a Bardeen-Cooper-Schrieffer superconductor, J. Phys.: Condens. Matter **19**, 486211 (2007).

[24] T. Meng, S. Florens, and P. Simon, Self-consistent description of andreev bound states in josephson quantum dot devices, Phys. Rev. B **79**, 224521 (2009).

[25] D. Futterer, M. Governale, M. G. Pala, and J. König, Nonlocal andreev transport through an interacting quantum dot, Phys. Rev. B **79**, 054505 (2009).

[26] J. Eldridge, M. G. Pala, M. Governale, and J. König, Superconducting proximity effect in interacting double-dot systems, Phys. Rev. B **82**, 184507 (2010).

[27] A. Braggio, M. Governale, M. G. Pala, and J. König, Superconducting proximity effect in interacting quantum dots revealed by shot noise, Solid State Commun. **151**, 155 (2011).

[28] G. Michałek, T. Domański, B. R. Bułka, and K. I. Wysokiński, Novel non-local effects in three-terminal hybrid devices with quantum dot, Sci. Rep. **5**, 14572 (2015).

[29] P. Trocha and I. Weymann, Spin-resolved andreev transport through double-quantum-dot cooper pair splitters, Phys. Rev. B **91**, 235424 (2015).

[30] R. Žitko, Numerical subgap spectroscopy of double quantum dots coupled to superconductors, Phys. Rev. B **91**, 165116 (2015).

[31] L. Bretheau, Ç. Ö. Girit, H. Pothier, D. Esteve, and C. Urbina, Exciting andreev pairs in a superconducting atomic contact, Nature (London) **499**, 312 (2013).

[32] B.-K. Kim, Y.-H. Ahn, J.-J. Kim, M.-S. Choi, M.-H. Bae, K. Kang, J. S. Lim, R. López, and N. Kim, Transport Measurement of Andreev Bound States in a Kondo-Correlated Quantum Dot, Phys. Rev. Lett. **110**, 076803 (2013).

[33] J.-D. Pillet, P. Joyez, R. Žitko, and M. F. Goffman, Tunneling spectroscopy of a single quantum dot coupled to a superconductor: From kondo ridge to andreev bound states, Phys. Rev. B **88**, 045101 (2013).

[34] A. Kumar, M. Gaim, D. Steininger, A. L. Yeyati, A. Martín-Rodero, A. K. Hüttel, and C. Strunk, Temperature dependence of andreev spectra in a superconducting carbon nanotube quantum dot, Phys. Rev. B **89**, 075428 (2014).

[35] E. J. H. Lee, X. Jiang, M. Houzet, R. Aguado, C. M. Lieber, and S. De Franceschi, Spin-resolved andreev levels and parity crossings in hybrid superconductor-semiconductor nanostructures, Nat. Nanotechnol. **9**, 79 (2014).

[36] J. Schindele, A. Baumgartner, R. Maurand, M. Weiss, and C. Schönenberger, Nonlocal spectroscopy of andreev bound states, Phys. Rev. B **89**, 045422 (2014).

[37] A. P. Higginbotham, S. M. Albrecht, G. Kirŝanskas, W. Chang, F. Kuemmeth, P. Krogstrup, T. S. Jespersen, J. Nygård, K. Flensberg, and C. M. Marcus, Parity lifetime of bound states in a proximitized semiconductor nanowire, Nat. Phys. **11**, 1017 (2015).

[38] L. Hofstetter, S. Csonka, J. Nygård, and C. Schönenberger, Cooper pair splitter realized in a two-quantum-dot y-junction, Nature (London) **461**, 960 (2009).

[39] L.G. Herrmann, F. Portier, P. Roche, A. L. Yeyati, T. Kontos, and C. Strunk, Carbon Nanotubes as Cooper-Pair Beam Splitters, Phys. Rev. Lett. **104**, 026801 (2010).

[40] J. Schindele, A. Baumgartner, and C. Schönenberger, Near-Unity Cooper Pair Splitting Efficiency, Phys. Rev. Lett. **109**, 157002 (2012).

[41] G. Fülöp, F. Domínguez, S. d'Hollosy, A. Baumgartner, P. Makk, M. H. Madsen, V. A. Guzenko, J. Nygård, C. Schönenberger, A. L. Yeyati, and S. Csonka, Magnetic Field Tuning and Quantum Interference in a Cooper Pair Splitter, Phys. Rev. Lett. **115**, 227003 (2015).

[42] J. Gramich, A. Baumgartner, and C. Schönenberger, Resonant and Inelastic Andreev Tunneling Observed on a Carbon Nanotube Quantum Dot, Phys. Rev. Lett. **115**, 216801 (2015).

[43] R. Leturcq, D. Graf, T. Ihn, K. Ensslin, D. D. Driscoll, and A. C. Gossard, Multi-terminal transport through a quantum dot in the coulomb-blockade regime, Europhys. Lett. **67**, 439 (2004).

[44] R. Leturcq, L. Schmid, K. Ensslin, Y. Meir, D. C. Driscoll, and A. C. Gossard, Probing the Kondo Density of States in a Three-Terminal Quantum Ring, Phys. Rev. Lett. **95**, 126603 (2005).

[45] A. Jacobsen, P. Simonet, K. Ensslin, and T. Ihn, Transport in a three-terminal graphene quantum dot in the multi-level regime, New J. Phys. **14**, 023052 (2012).

[46] A. Jacobsen, P. Simonet, K. Ensslin, and T. Ihn, Finite-bias spectroscopy of a three-terminal graphene quantum dot in the multilevel regime, Phys. Rev. B **89**, 165413 (2014).

[47] J. Gramich, A. Baumgartner, and C. Schönenberger, Subgap resonant quasiparticle transport in normal-superconductor quantum dot devices, Appl. Phys. Lett. **108**, 172604 (2016).

[48] W. Chang, V. E. Manucharyan, T. S. Jespersen, J. Nygård, and C. M. Marcus, Tunneling Spectroscopy of Quasiparticle Bound States in a Spinful Josephson Junction, Phys. Rev. Lett. **110**, 217005 (2013).

[49] A. Jellinggaard, K. Grove-Rasmussen, M. H. Madsen, and J. Nygård, Tuning yu-shiba-rusinov states in a quantum dot, Phys. Rev. B **94**, 064520 (2016).

[50] Y. Tanaka, N. Kawakami, and A. Oguri, Numerical renormalization group approach to a quantum dot coupled to normal and superconducting leads, J. Phys. Soc. Jpn. **76**, 074701 (2007).

[51] J. Barański and T. Domański, In-gap states of a quantum dot coupled between a normal and a superconducting lead, J. Phys.: Condens. Matter **25**, 435305 (2013).

[52] G. Sellier, T. Kopp, J. Kroha, and Y. S. Barash, π junction behavior and Andreev bound states in Kondo quantum dots with superconducting leads, Phys. Rev. B **72**, 174502 (2005).

[53] E. J. H. Lee, X. Jiang, R. Žitko, R. Aguado, C. M. Lieber, and S. de Franceschi, Scaling of sub-gap excitations in a superconductor-semiconductor nanowire quantum dot, Phys. Rev. B **95**, 180502 (2017).

[54] J. Samm, J. Gramich, A. Baumgartner, M. Weiss, and C. Schönenberger, Optimized fabrication and characterization of carbon nanotube spin valves, J. Appl. Phys. **115**, 174309 (2014).

[55] J. Nygård, D. H. Cobden, and P. E. Lindelof, Kondo physics in carbon nanotubes, Nature (London) **408**, 342 (2000).

[56] B. Babić, T. Kontos, and C. Schönenberger, Kondo effect in carbon nanotubes at half filling, Phys. Rev. B **70**, 235419 (2004).

[57] D. Sánchez and R. López, Three-terminal transport through a quantum dot in the kondo regime: Conductance, dephasing, and current-current correlations, Phys. Rev. B **71**, 035315 (2005).

[58] F. D. M. Haldane, Scaling Theory of the Asymmetric Anderson Model, Phys. Rev. Lett. **40**, 416 (1978).

[59] Y.-h. Zhang, S. Kahle, T. Herden, C. Stroh, M. Mayor, U. Schlickum, M. Ternes, P. Wahl, and K. Kern, Temperature and magnetic field dependence of a kondo system in the weak coupling regime, Nat. Commun. **4**, 2110 (2013).

[60] P. Jarillo-Herrero, J. Kong, H. S. J. van der Zant, C. Dekker, L. P. Kouwenhoven, and S. De Franceschi, Orbital kondo effect in carbon nanotubes, Nature (London) **434**, 484 (2005).

[61] M. R. Buitelaar, T. Nussbaumer, and C. Schönenberger, Quantum Dot in the Kondo Regime Coupled to Superconductors, Phys. Rev. Lett. **89**, 256801 (2002).

[62] A small offset between the current to voltage converters results in the small deviation from $V_2 = 0$.

[63] K. Izydor Wysokiński, Thermoelectric transport in the three terminal quantum dot, J. Phys.: Condens. Matter **24**, 335303 (2012).

[64] L. Rajabi, C. Pöltl, and M. Governale, Waiting Time Distributions for the Transport through a Quantum-Dot Tunnel Coupled to One Normal and One Superconducting Lead, Phys. Rev. Lett. **111**, 067002 (2013).

[65] G. Fülöp, S. d'Hollosy, A. Baumgartner, P. Makk, V. A. Guzenko, M. H. Madsen, J. Nygård, C. Schönenberger, and S. Csonka, Local electrical tuning of the nonlocal signals in a cooper pair splitter, Phys. Rev. B **90**, 235412 (2014).

[66] C. Livermore, C. H. Crouch, R. M. Westervelt, K. L. Campman, and A. C. Gossard, The Coulomb blockade in coupled quantum dots, Science **274**, 1332 (1996).

[67] W. G. van der Wiel, S. De Franceschi, J. M. Elzerman, T. Fujisawa, S. Tarucha, and L. P. Kouwenhoven, Electron transport through double quantum dots, Rev. Mod. Phys. **75**, 1 (2002).

[68] G. Fábián, P. Makk, M. H. Madsen, J. Nygård, C. Schönenberger, and A. Baumgartner, Magnetoresistance engineering and singlet/triplet switching in inas nanowire quantum dots with ferromagnetic side gates, Phys. Rev. B **94**, 195415 (2016).